Kinetics of Surface and Interfacial Fluctuations in Phase Separating Polymer Blend Films

Howard Wang* and Russell J. Composto

Department of Materials Science and Engineering, Laboratory for Research on Structure of Matter, University of Pennsylvania, Philadelphia, Pennsylvania 19104

Received September 24, 2001

ABSTRACT: Surface and interfacial fluctuations in phase separating thin film polymer blends are investigated using atomic force microscopy (AFM) and forward recoil spectrometry. The root-mean-square roughness at the surface ($R_{q,s}$) and the interface beneath the wetting layer ($R_{q,i}$) are quantified using AFM. $R_{q,s}$ is found to scale with the initial film thickness (l_0) during the early and intermediate stages, consistent with the morphology evolution mechanism reported earlier; however, the entire temporal evolution of $R_{q,s}$ does not scale with l_0. A fast Fourier transform of the AFM images uncovers low (q_l) and high (q_h) wavenumber fluctuations at both the surface and interface. The former fluctuation is associated with capillary fluctuations, whereas the latter reflects spinodal decomposition within the film. As the minority phase in the bulk of films undergoes 2D coarsening, the high wavenumber surface and interface fluctuations follow power-law dynamics, $q_{h,s} \sim t^{\alpha_s}$ and $q_{h,i} \sim t^{\alpha_i}$, respectively. Both $-\alpha_s$ and $-\alpha_i$ increase with film thickness and reach an asymptotic value of about $^1/_3$, suggesting that decreasing film thickness inhibits the growth of short wavelength fluctuations. Furthermore, $-\alpha_s$ is systematically less than $-\alpha_i$, suggesting that the surface fluctuations are hindered relative to interfacial ones and that the surface and internal fluctuations are not conformal.

Introduction

Understanding the morphology of thin film polymer blends, sometimes with additives, is important to applications ranging from biomedical (e.g., coatings on contact lenses) to electronics (e.g., lithography). Because polymers are generally incompatible, the effect of finite film thickness, or confinement, on phase segregation parallel and perpendicular to the surface is of great importance.[1] In particular, the morphology of confined binary polymer blends undergoing spinodal decomposition has received much recent attention; these studies have revealed a variety of morphologies, including films that are smooth or rough, contain bicontinuous or discrete (i.e., droplet) phases, or display stratified or perforated layers depending on the geometry and system.[2−25] The observation of these diverse morphologies can be partly attributed to the effect of confinement on thermodynamics, phase separation kinetics, and/or interfacial fluctuations.

The thermodynamics and kinetics of thin films can be perturbed by geometric confinement.[26−31] For example, surface interactions and/or confinement have been shown to shift the critical temperature, which in turn will perturb the driving force for phase separation.[26−31] Wetting and confinement can also break the symmetry of composition fluctuations, resulting in surface-directed spinodal decomposition (SDSD).[8] In addition, the characteristic wavevector parallel to the surface can grow faster than the perpendicular component, and both may differ from their bulk values.[32,33] Using numerical simulations,[26−28,32−37] composition fluctuations normal and parallel to the surface have been shown to be perturbed by confinement at relatively early times of phase separation. Quantitative experimental support for these predictions is currently lacking. On the other hand, experiments have revealed a fascinating zoology of late stage morphologies.[2−23] However, because they lack surface roughening and/or hydrodynamic interactions, current numerical simulations[26−28,32−37] are unable to adequately predict the full zoology of structures. In part, this article bridges the gap between models and experiments, while providing new experimental evidence for the mechanisms underlying fluctuations in thin film polymer blends.

Previously, we reported that a critical composition, thin film polymer blend follows a distinct morphological pathway during phase separation that eventually leads to a rough film with droplets of the nonwetting phase encapsulated by the wetting phase.[25] In particular, the evolution is characterized by an early stage dominated by hydrodynamic wetting and the formation of a trilayer structure, an intermediate stage involving backflow of the surface wetting component and simultaneous 2D phase coarsening within the middle (nonwet) layer, a transition stage denoted by rupture of the middle layer due to the capillary fluctuations, and finally a late stage characterized by spinodal dewetting and lateral phase coarsening. The final film is quite rough because the encapsulated droplets of the nonwetting phase protrude from the surface, as reported elsewhere.[5,15−17] This evolution pathway is denoted as "class A" for convenience.

For a critical binary blend, class A evolution was observed for films ranging from 100 to 1500 nm (∼10 to 150 R_g, the radius of gyration), where both length and time scales during the morphology evolution depend on film thickness. However, other evolution pathways may be possible if one explores the vast parameter space, which includes thickness, composition, temperature, viscosity, substrate type, environment, etc. For example, the same critical blend displays three other pathways as the film thickness decreases from semi-infinite to below R_g.[38] More detailed studies of class A

* Corresponding author. Current address: NIST, Gaithersburg, MD, e-mail hao.wang@nist.gov.

10.1021/ma0116699 CCC: $22.00
Published on Web 03/03/2002

evolution are important for understanding (1) other evolution pathways, (2) phase separation on microscopically[39−41] or nanoscopically[42] patterned substrates, and (3) pattern formation during spin-casting and subsequent morphology evolution.[43]

In this article, we quantify compositional fluctuations both perpendicular and parallel to the surface of class A thin films ranging from 100 to 500 nm. Because of their relatively slow growth, the amplitude and wavelength of fluctuations can be measured over more than 2 decades of time during the early and intermediate stages of phase evolution (i.e., prior to rupture). Upon selectively removing the wetting phase, the fluctuation characteristics along the wetting/nonwetting interface are revealed for the first time. Previously,[48] we briefly reported the observation of short and long lateral fluctuations in 223 nm films which were attributed to phase separation and capillary fluctuations, respectively. Here, we provide a detailed analysis of the thickness dependence of both features at the surface and the interface. In contrast to a recent model attributing thin film rupture to phase coarsening,[23] our analysis shows that "spinodal-like" interfacial fluctuations are mainly responsible for rupture. We observe that the length scales of phase separation and capillary fluctuations both develop in stages. Whereas the phases evolve from 3D (bulk) to 2D (confined) behavior, capillary fluctuations display three stages as they develop, become pinned, and then cause rupturing and dewetting. In particular, the short wavelength characteristic of phase separation follows power-law dynamics whose exponent is smaller at the surface than at the interface although both increase asymptotically toward $^1/_3$ as film thickness increases. This is attributed to the confinement effect on phase separation, more specifically, the effect of film thickness on asymmetric coarsening of the phase domains in thin films.[3,4]

Experiment

The polymers are deuterated poly(methyl methacrylate) (dPMMA) and poly(styrene-*ran*-acrylonitrile) (SAN) having an AN content of 33 wt %. The weight-average molecular weight and polydispersity of dPMMA and SAN are 90 kg/mol and 1.06 and 124 kg/mol and 2.24, respectively. Their blend exhibits lower critical solution behavior with a critical temperature and composition of ca. 160 °C and ca. 0.48, respectively. All thin film samples contain a critical concentration with 50% mass fraction of dPMMA. Three solutions of methyl isobutyl ketone, dPMMA, and SAN with different polymer concentrations were spun-cast on silicon at 2000 rmp. After preannealing at 120 °C for 24 h, the resulting films were 108, 223, and 495 nm, as measured by ellipsometry. They are denoted as samples T1, T2, and T5, respectively. To prepare consistent substrate surfaces, the native oxide layer of the as-received silicon was removed using a buffered HF solution; a new oxide layer was then grown on the silicon by exposure to ultraviolet radiation and ozone.

After annealing films at 185 °C in argon for various times, the depth profile and morphology were examined by forward recoil spectrometry (FRES) and atomic force microscopy (AFM), respectively. Experimental details have been reported previously.[25] In FRES, MeV He^{2+} or He^{+} ions impinged on the sample at a grazing angle. Deuterium and hydrogen atoms were elastically recoiled from the film, and their energy, after passing a Mylar stopper foil, was determined by a solid-state detector. To optimize depth resolution and probing depth at each film thickness, 1.0 and 2.0 MeV He^{+} ions and 2.85 MeV He^{2+} ions were used for T1, T2, and T5, respectively. The stopper was a 3.0 μm Mylar foil for 1.0 MeV ions and an 8.0 μm Mylar foil for the higher energy ions. The depth resolution

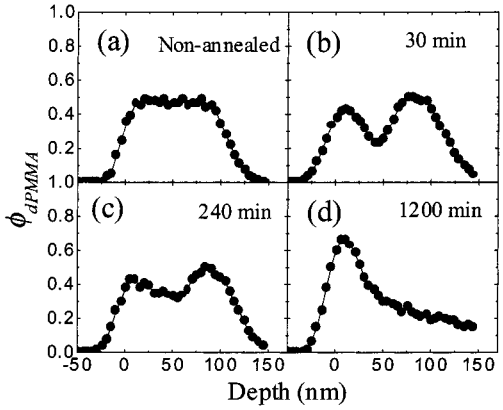

Figure 1. FRES depth profiles of dPMMA after annealing T1 at 185 °C. (a) Before annealing, the sample is homogeneous. (b) After 30 min, a trilayer structure of dPMMA-rich/SAN-rich/dPMMA-rich forms. (c) After 240 min, the layered structure decays, and the overall volume fraction profile appears more homogeneous than in (b). (d) After 1200 min, the surface layer grows to a thickness of about 40 nm and is followed by a dPMMA-depleted region.

at the surface, defined as the fwhm, was ca. 80, 40, and 16 nm for the 2.85, 2.0, and 1.0 MeV ions, respectively. The morphology of both the surface and the interface was examined using a Digital Instrument Dimension 3000 atomic force microscope at room temperature. The interfacial morphology was exposed by selectively removing the dPMMA-rich phase. The root-mean-square roughness, R_q, was calculated from the image using Nanoscope III software,

$$R_q = \left[\frac{\oint\oint [h(x,y) - h_0]^2 \, dA}{\oint\oint dA}\right]^{0.5} \quad (1)$$

where the integrations were over the areas and $h(x,y)$ was the height function, and the reference height h_0 is defined as

$$h_0 = \frac{\oint\oint h(x,y) \, dA}{\oint\oint dA} \quad (2)$$

The image size for calculating R_q was much larger than the largest feature size, hence eliminating the image size dependence of the roughness such as for fractal surfaces.

In this study, more than 60 samples were used for different thickness, annealing times, and surface and interface studies. The consistent behavior of many samples suggests that measurements are highly reproducible.

Results and Discussion

1. Depth Profile and Morphology. Figure 1 shows the dPMMA volume fraction profiles of T1 after annealing at 185 °C. Initially, the composition is homogeneous (Figure 1a). After 30 min (Figure 1b), dPMMA-rich wetting layers form at the surface and substrate, resulting in a trilayer structure. With further annealing (Figure 1c), the dPMMA profile appears more uniform as the surface layer thins. After 1200 min (Figure 1d), a dPMMA-rich layer of ca. 40 nm, about half the initial thickness, forms at the surface. The diffuse dPMMA profile below 50 nm indicates that the film has become rough, as verified by AFM studies.

Figure 2 shows the topology of the surface (left column) and the SAN-rich phase (right column) for T1 after 10 min (a and b), 30 min (c and d), 480 min (e and f), and 6000 min (g and h). The relative height scales with the gray level, where light and dark regions are high and low, respectively. For each time, the height and lateral dimensions are chosen in order to optimize

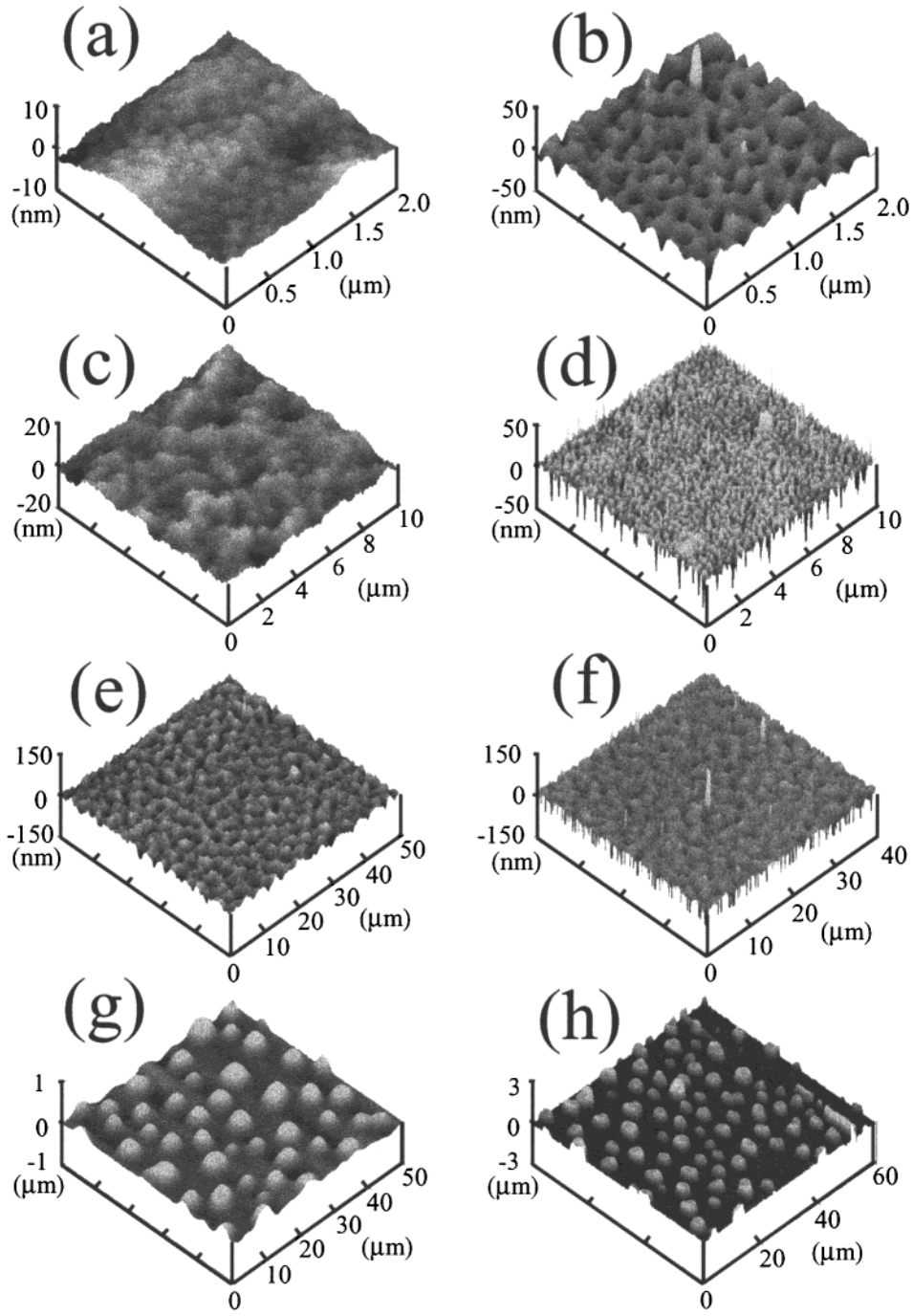

Figure 2. AFM images of the surface (left column) and interface morphology (right column) at 185 °C for T1 after 10 min (a and b), 30 min (c and d), 480 min (e and f), and 6000 min (g and h). The gray level depicts the height scale, where light and dark regions correspond to high and low features, respectively. To resolve features, the lateral and height scales have been optimized for each image.

the surface and interface features. After 10 min, the surface roughens by the growth of small hills as shown in Figure 2a, whereas the region right beneath the surface layer displays a bicontinuous structure (Figure 2b). After 30 min (Figure 2c), long wavelength (micrometers) and small amplitude (nanometers) fluctuations start to develop. Upon close inspection, Figure 2c also reveals short wavelength features similar to those observed on the interface shown in Figure 2d. Figure 2d shows that the majority phase in the middle layer is SAN-rich and that the small length scale features reflect dPMMA-rich domains that span the surface and substrate wetting layers, as seen from the edge (cross section) of Figure 2d. After 480 min, the surface displays bicontinuous large-scale fluctuations (Figure 2e). In contrast to images 2a−b and 2c−d, the surface (Figure 2e) and interface (Figure 2f) fluctuations display similar length scales. After 6000 min, both the surface (Figure 2g) and interface (Figure 2h) exhibit droplet morphology. Although difficult to observe in Figure 2h, the SAN-rich droplets show a depression at the top. The concave droplet shape is absent in both the thinner and thicker films and will be discussed in a later publication.[38]

Figures 3 and 4 show the depth profile and topology, respectively, of T2. Figure 3a shows that the initial film is homogeneous. After 60 min, the film separates into a trilayer structure (Figure 3b), similar to T1. After 1200 min, the dPMMA volume fraction profile again appears

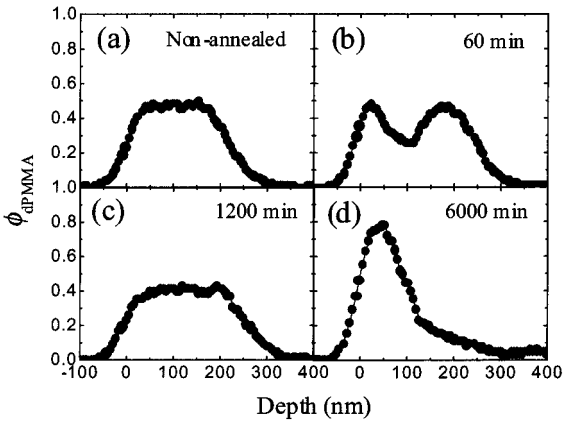

Figure 3. FRES depth profiles of dPMMA after annealing T2 at 185 °C. (a) Before annealing, the sample is homogeneous. (b) After 60 min, a trilayer structure of dPMMA-rich/SAN-rich/dPMMA-rich forms. (c) After 1200 min, the layered structure decays and the overall volume fraction profile appears homogeneous. (d) After 6000 min, the surface layer grows to a thickness of about 100 nm and is followed by a dPMMA-depleted region.

uniform as shown in Figure 3c. After 6000 min, a dPMMA-rich layer, ca. 100 nm, appears at the surface as shown in Figure 3d. The diffuse profile below 100 nm suggests surface roughening. Figure 4 shows the topology of the surface (left column) and the interface (right column) for T2 after 10 min (a and b), 60 min (c and d), 2700 min (e and f), and 6000 min (g and h). Although their spatial and temporal scales differ, the main features shown in Figure 4 are qualitatively the same as those exhibited by T1 in Figure 2. Figure 4c is of particular interest because both the short-wavelength/small-amplitude and long-wavelength/large-amplitude fluctuations are captured simultaneously at 60 min. After 2700 min, Figure 4f shows that the nonwetting SAN-rich phase forms a long-wavelength 2D interconnected structure punctured with holes. The origin of these holes is apparent from the 5 μm × 5 μm area scan shown in Figure 4d. Quantification of the characteristic length scales, such as surface hills, capillary fluctuations, and droplets, will be presented later.

The new results describing the behavior of T1 (108 nm) and T2 (223 nm) are in excellent agreement with the evolutionary stages exhibited by T5 (495 nm), a system that has been analyzed in detail.[25] Selective studies on films thicker than T5 suggest that the morphology and depth profile for films ranging from 100 to 1500 nm, or about 10 to 150 R_g, where R_g is the radius of gyration, display three distinct stages of evolution. Upon quenching into the two-phase regime, the initially homogeneous film undergoes simultaneous spinodal decomposition and wetting. The early stage is characterized by the rapid formation of a dPMMA-rich wetting layer at the surface that is driven by hydrodynamic flow through the underlying bicontinuous phase morphology in the near surface region. By the end of this stage, a trilayer-like structure forms with dPMMA-rich layers at both the free film surface and the film/silicon oxide interface and an SAN-rich layer in the middle. During the intermediate stage, dPMMA-rich domains in the middle layer coarsen while dPMMA flows from the wetting layers into the bulk. Because FRES provides a depth profile averaged over 1 mm × 3 mm, the dPMMA volume fraction across the two-phase structure appears uniform (cf. Figure 3c). During this stage, capillary fluctuations begin to dominate, causing the film thickness to undulate. Eventually the amplitude of fluctuations becomes large enough to rupture the middle layer, resulting in an interconnected 2D network (cf. Figures 2f and 4f). Simultaneously, the dPMMA-rich phase flows from the domains in the middle layer into the wetting layer at the surface. During the late stage, the 2D network coarsens and eventually forms isolated droplets of SAN-rich phase covered by a thick dPMMA-rich layer (cf. Figure 2f−h and Figure 4f−h). This novel evolution is attributed to the dynamic interplay between wetting, phase separation, capillary fluctuation, hydrodynamic flow, and confinement.

Table 1. Surface Roughness Characteristics

sample	t_p (min)	$R_{q,p}$ (nm)	t_r (min)	t_i (min)	Δt_p (min)	$R_{q,f}$ (nm)
T1	50	2	270	600	100	90
T2	100	4	1260	1500	400	150
T5	250	12	3160	3500	2500	250

Although T1, T2, and T5 exhibit similar stages of development, the rate of evolution for each stage decreases as film thickness increases. For example, the trilayer structure, signifying the end of the early stage, is formed after ca. 30, 60, and 120 min for T1, T2, and T5, respectively. The end of the intermediate stage coincides with the apparent homogeneous dPMMA profile and is observed after 480, 1200, and 2880 min for T1, T2, and T5, respectively. The third stage, corresponding to the final droplet morphology, is established at around 1200, 6000, and 15 720 min for T1, T2, and T5, respectively. A quantitative analysis of the effect of thickness on the kinetics of evolution will be discussed below.

2. Roughness. 2.1. Surface Roughness. Figure 5 shows how the surface roughness, $R_{q,s}$, increases with time for T1 (squares), T2 (circles), and T5 (crosses). The solid lines are B-spline fits to guide the eye, and the inset shows early time behavior. The development of $R_{q,s}$ is similar for all three samples. Namely, $\log(R_{q.s})$ increases rapidly, initially, and then reaches a plateau (inset). After the plateau, $R_{q,s}$ increases again before approaching a final roughness value. During the initial roughening process, $R_{q,s}$ is quite small relative to the initial film thickness, l_0. However, the second roughening process leads to macroscopic roughness values comparable to l_0. In Figure 5, the thickest film shows the largest roughness values during the initial and late times; however, at an intermediate time, its roughness is less than the thinner ones. This behavior can be explained using a scaling analysis as discussed below.

Before testing scaling, spatial, and temporal characteristics of the roughening process are first defined in Figure 6A. The onset time t_p and roughness $R_{q,p}$ of the first plateau are represented by the solid circle. The time to rupture t_r (solid triangle) is defined when the film crosses from constant wavelength fluctuations to late stage lateral coarsening. The values of t_r are obtained from Figure 9. This time coincides with the onset of the second roughening process. The width of the plateau Δt_p is the difference between t_r and t_p. The inflection point of the second roughening process denotes the inflection time t_i (solid square). The final roughness is $R_{q,f}$. The values of these parameters are listed in Table 1.

The initial roughening process is attributed to (1) phase separation in the bulk of the film and (2) hydrodynamic flow driven wetting. During spinodal decomposition, a bicontinuous morphology in the film generates a pressure gradient, causing the dPMMA-rich

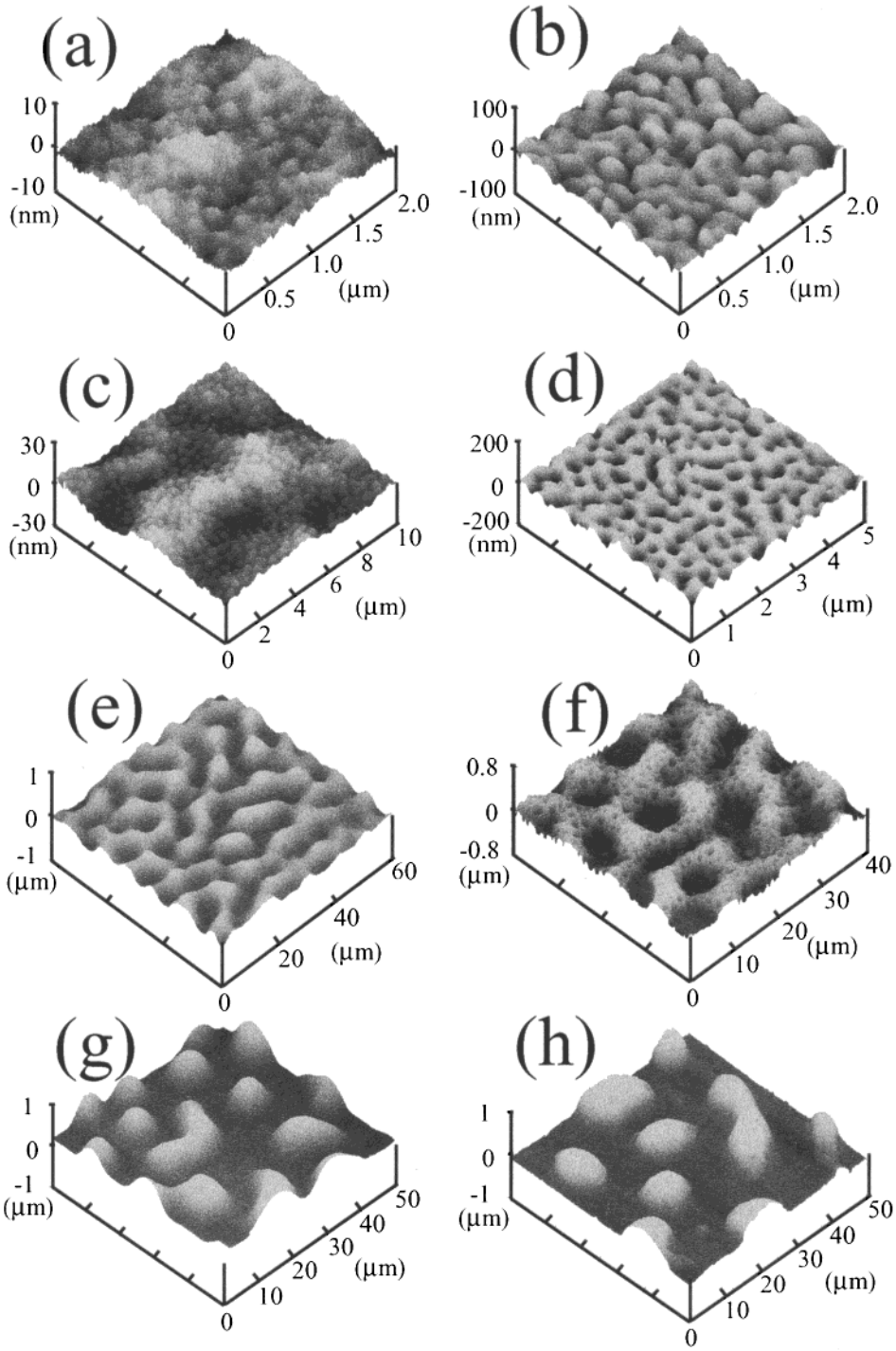

Figure 4. AFM images of the surface (left column) and interface morphology (right column) at 185 °C for T2 after 10 min (a and b), 60 min (c and d), 2700 min (e and f), and 6000 min (g and h). The gray level depicts the height scale, where light and dark regions correspond to high and low features, respectively. Each image has its own lateral and height scale.

phase to wet the surface via hydrodynamic flow; in response to this pressure, surface hills develop over the dPMMA-rich interconnected channels that reach the wetting layers.[19,24] These hills are approximately the same size as the underlying channels and, therefore, reflect the internal phase structure of the film.[25] As the phase size approaches l_0, the pressure gradient relaxes, and this initial roughening mechanism slows down. Thus, the first plateau results from film stabilization due to confinement. During hydrodynamic phase coarsening, the characteristic length increases linearly with time.[25] Therefore, t_p should scale linearly with l_0. Because the dimensions of the wetting channels determine the size of surface hills, $R_{q,p}$ should also increase linearly with l_0. For T1, T2, and T5, Table 1 shows that the relative values of t_p and $R_{q,p}$ are 1:2:5 and 1:2:6, respectively, in excellent agreement with the normalized thickness 1:2:5. Thus, during the first stage, the linear scaling of both the time and spatial evolution of roughening with initial film thickness is consistent with a roughening mechanism due to phase separation.

The plateau regime coincides with backflow of the dPMMA-rich phase from the surface wetting-layer into cylindrical domains in the middle layer. This back-flow is driven by capillary pressure originating from the interfacial curvature between phases in the middle

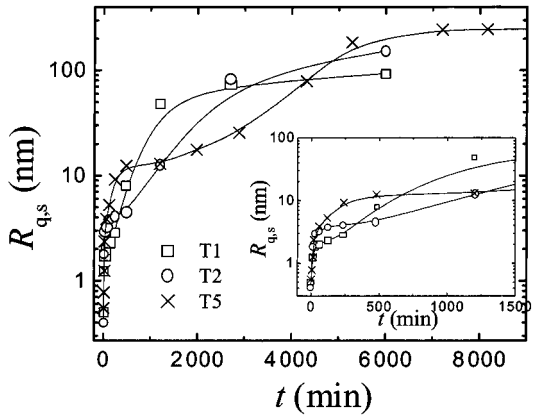

Figure 5. Root-mean-square roughness, $R_{q,s}$, of the surface as a function of time for T1 (squares), T2 (circles), and T5 (crosses). The solid curves are B-spline curve fits to guide the eye. The $\log(R_{q,s})$ initially increases rapidly, reaches a plateau, increases rapidly again, and then reaches a final plateau. The inset shows the early time behavior of $R_{q,s}$ for the three samples. The symbols are consistent with the main figure.

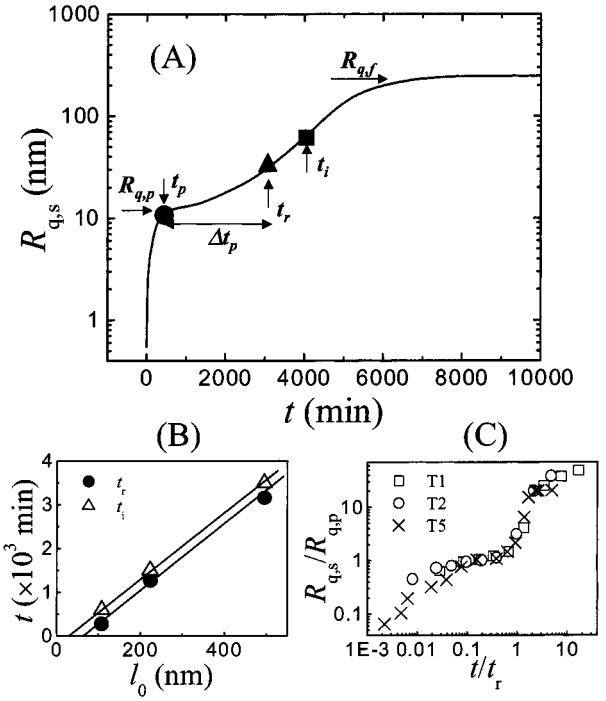

Figure 6. (A) A representative plot of the roughness evolution defining: the roughness and onset time of the first plateau regime, $R_{q,p}$ and t_p, respectively (circle); the width of the plateau, Δt_p, which ranges from the onset of the plateau to the onset of the second roughening process, t_r; the time at the inflection of the second roughening process, t_i, which characterizes the onset of lateral phase pinning; and the final sample roughness $R_{q,f}$. (B) The film thickness dependence of t_r and t_i, both roughly follow a linear relationship. (C) The dynamic scaling of $R_{q,i}$ in reduced coordinates. A master curve is followed by all samples except at initial and late times.

layer.[25] The domain diameter D is described by $dD/dt \sim (\sigma/\eta)(2/h)$, where σ and η are the interfacial tension and viscosity and h is the thickness of the middle SAN-rich (majority phase) layer. During back-flow, the area fraction of the dPMMA-rich phase in the middle layer increases from 0.24 to 0.35,[25] and therefore, by conservation of mass, h varies from ca. $0.66l_0$ to $0.77l_0$. So the domain diameter when the back flow terminates scales as $D_f \sim \Delta t_p/l_0$. Because the cylinder density N scales as $t^{-2/3}$ and conservation of wetting material requires

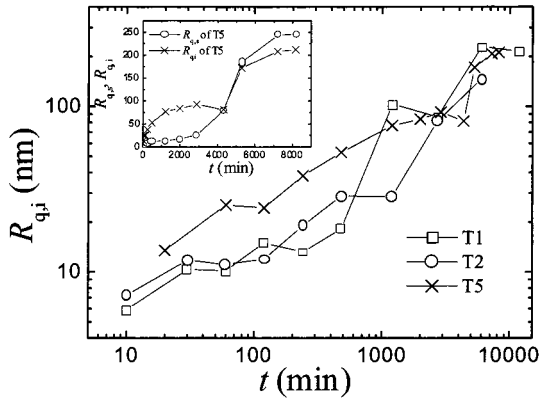

Figure 7. Root-mean-square roughness of the interface between the wet and nonwet layers, $R_{q,i}$, as a function of time for T1 (squares), T2 (circles), and T5 (crosses). $R_{q,i}$ behaves similar to $R_{q,s}$ in Figure 5 One distinct feature of $R_{q,i}$ is that it levels off and becomes slightly depressed before the final roughness stage. The inset compares $R_{q,s}$ (circles) with $R_{q,i}$ (crosses) for T5 and reveals that the $R_{q,i}$ depression coincides with the inflection point of the final roughening process of $R_{q,s}$.

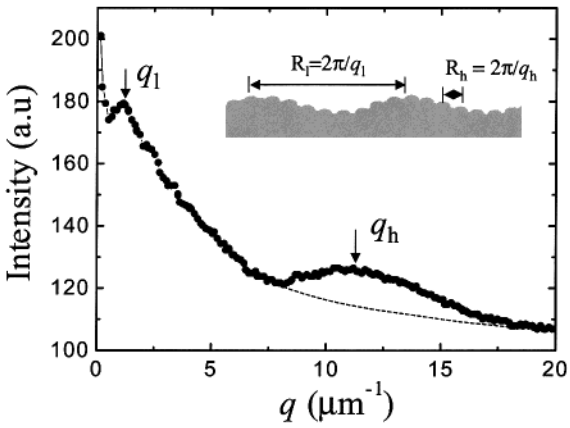

Figure 8. Radial-averaged 2D FFT intensity as a function of wavevector for T2 after 60 min at 185 °C. Peaks are observed at low and high q, denoted as q_l and q_h, respectively. The dash line approximates the background intensity. The inset schematically shows the coexistence of two length scales, with their characteristic length, $R_i = 2\pi/q_i$, where i represents l or h.

$ND_f^2 \sim l_0$,[25] we have $(D_f l_0)^{-2/3} D_f^2 \sim l_0$ or $D_f \sim l_0^{5/4}$. Therefore, the plateau period can be described by $\Delta t_p \sim l_0^{9/4}$. From the measured value in Table 1, Δt_p is found to scale as l_0^2. This result is in qualitative agreement with a scaling analysis based on capillary forces.

The second roughening stage is due to capillary wave fluctuations, which are driven by attractive forces between the dPMMA-rich/SAN-rich interfaces separating the middle SAN-rich membrane. According to capillary fluctuation theory[44–46] and experiments on simple films,[47] the characteristic time for breaking a film scales as h_0^5, where h_0 is the initial film thickness. In our study, h_0 corresponds to the thickness of the middle SAN-rich layer, h, which is approximately proportional to l_0. Based on this analysis, the time to rupture T5 and T2 should be 2023 and 38 times longer than T1, the thinnest film. However, Table 1 gives relative times of 11.8 and 4.7, demonstrating that films rupture much faster than predictions based on capillary wave theory. There are several possible reasons for this discrepancy. First, lateral phase coarsening can enhance capillary wave development by a positive feedback mechanism.[25] Second, the thickness of the middle layer changes with time, decreasing and increasing during the early and

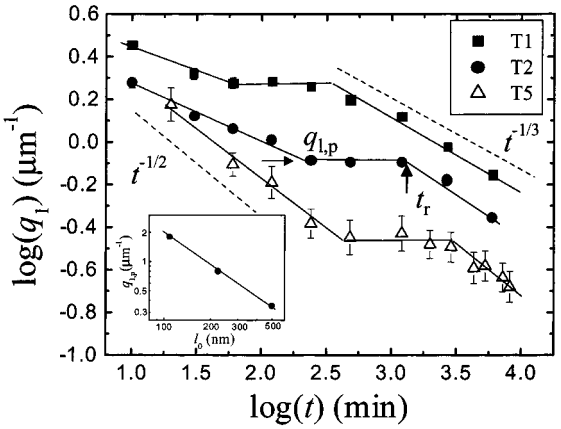

Figure 9. Low q wavevector, q_l, for T1 (solid squares), T2 (solid circles), and T5 (open triangles), obtained by FFT (T1 and T2) and RSM (T5) methods. The solid lines through the data points are to guide the eye. The dash lines represent $t^{-1/3}$ and $t^{-1/2}$ behavior. All films display a three-stage evolution pattern; two power-law regimes separated by a plateau. The inset shows the plateau wavevector, $q_{l,p}$, varies as l_0^{-1}. The crossover time from plateau to later stage coarsening is denoted as t_r (see Figure 6). Note that some error bars for the filled symbols are smaller than the symbol size itself.

late stages, respectively. Third, the capillary theory formalism[44−46] assumes a homogeneous film at its equilibrium thickness. Note, the faster than exponential growth of $R_{q,s}$ during the second roughening process already suggests the breakdown of the theory.

Figure 6B (Table 1) shows that t_r and t_i increase nearly linearly with l_0. Recall that t_r and t_i denote the times for film rupture and the onset of finite thickness confinement on late stage coarsening, respectively. Thus, their linear relationship with l_0 suggests a similar underlying mechanism, namely a capillary pressure driven instability. Hoppe, Heuberger, and Klein[23] also found that t_r scales with film thickness for a copolymer blend of diethyl and ethylethylene monomers. Observing only a single dominate lateral fluctuation, they attribute the rupture mechanism to the coarsening of the bicontinuous structure (i.e., phase separation). Extrapolation of the data in Figure 6B to t_r (or t_i) = 0 results in a positive value of l_0, suggesting a critical thickness below which class A evolution breaks down.[38] Figure 6C shows the reduced roughness $R_{q,s}/R_{q,p}$ as a function of reduced time t/t_r. Except for the very early and late times, all three data sets fall approximately on a master curve during the plateau and second roughening process. The lack of a global scaling rule for the entire time regimes reflects the change in the dominant morphology mechanisms during evolution. Specifically, the early stage shows that thinner films display an increasing confinement effect on phase separation, resulting in a smaller plateau roughness, $R_{q,p}$, and therefore a larger reduced roughness at early times. During the late stage, $R_{q,s}$ ($=R_{q,f}$) is less than expected in thicker films because larger droplets take longer to achieve their equilibrium height (i.e., kinetic trapping). Figure 5 (Table 1) shows that $R_{q,f}$ increases from 90 to 150 to 250 nm. However, a quantitative analysis of $R_{q,f}$ as a function of l_0 is problematic because the kinetic trapping (pinning) of droplets increases as film thickness increases, as discussed in a later publication.[38]

2.2. Interfacial Roughness. The root-mean-square interfacial roughness, $R_{q,i}$, for T1, T2, and T5 is shown in Figure 7. The solid lines are to guide the eye. Qualitatively similar to $R_{q,s}$ (Figures 5 and 6), $R_{q,i}$ increases from microscopic ($<l_0$) to macroscopic ($\sim l_0$) values during annealing. However, distinct stages of lateral evolution are not observed at the interface between the wetting and middle layer. This behavior may be attributed to the dynamic complexity (e.g., multiple or coupled mechanisms) driving the evolution of internal features; thus, finer time intervals may be needed to reveal the individual stages. One observation that suggests interesting internal dynamics is the suppression of $R_{q,i}$ prior to the final roughness plateau. To accentuate this suppression, the inset compares the growth of $R_{q,s}$ and $R_{q,i}$ on a linear time axis for T5. The solid lines are to guide the eye. Note that $R_{q,i}$ reaches a minimum at 4320 min, which is the same time that $R_{q,s}$ reaches its inflection point signifying film rupture. The slight depression of $R_{q,i}$ can be attributed to the ejection of the trapped dPMMA-rich phase from the SAN-rich matrix, hence smoothing the interface.[25]

Figure 7 also shows that film thickness has some effect on $R_{q,i}$. Initially, thicker films generally have a larger interfacial roughness because feature height scales with film thickness. However, at later times (>2000 min), $R_{q,i}$ does not vary significantly between samples. One explanation is that domain pinning in thicker films retards the height of droplets and therefore offsets the thickness effect.

3. Lateral Fluctuations. 3.1. Introduction. In a previous study, phase separation of sample T2 was found to display two evolving lateral length scales at both the free film surface and the interface.[48] Here, the short-wavelength mode obeyed a power law growth at both the surface and interface, but with a smaller growth exponent at the surface, implying slower kinetics. The long-wavelength mode was found to display two power law growth regimes separated by a plateau. We extend our studies to thicker and thinner films to determine whether these two lateral length scales are indeed general to polymer blend thin films undergoing class A evolution. Furthermore, we explore whether the growth exponents are a function of film thickness.

To determine the lateral length scales, a fast Fourier transform (FFT) of the AFM surface and interface images is taken. Figure 8 shows the radial averaged FFT of the AFM surface morphology shown in Figure 4c for T2. The two arrows denote the maximum wavevectors at low- and high-q positions, q_1 and q_h, respectively, or correspondingly the long and short characteristic wavelengths shown in the inset of Figure 8. The long wavelength $R_l = 2\pi/q_l$ reflects capillary fluctuations, whereas the short wavelength $R_h = 2\pi/q_h$ characterizes length scales reflecting the phase morphology. In Figure 8, q_1 and q_h are 1.0 and 11.3 μm^{-1}, respectively, or R_l = 6.3 μm and R_h = 0.56 μm.

Because the long wavelength fluctuations in T5 are very large, the wavevector cannot be obtained from a FFT due to poor statistics. Therefore, the wavelength was determined by a real space measurement (RSM) from the AFM images using the distance between neighboring high or low regions. The wavelength of the surface fluctuations was obtained by averaging 30−50 measurements per sample. For selected samples, q_1 values were determined by both FFT and RSM and found to be within experimental error. In the following sections, we discuss the evolution of q_1 and q_h.

3.2. Low Wavenumber Fluctuations, q_l. On a log−log plot, Figure 9 shows how the surface q_l varies with

time for T1, T2, and T5. The error bars for T5 reflect the uncertainty of the RSM method. At a particular time, the wavenumber decreases with increasing thickness. Namely, the wavelength of fluctuations increases as confinement effects are relaxed. For all samples, q_l displays three distinct stages of evolution corresponding to early and late power law regimes separated by a plateau. As a reference, $t^{-1/3}$ and $t^{-1/2}$ power law dependences are plotted as dashed lines. The late stage evolution approximately follows a $t^{-1/3}$ power law for all samples, whereas the early stage kinetics increases systematically from about $t^{-1/4}$ for T1 to $t^{-1/2}$ for T5. The interface q_l matches the magnitude and time dependence of the surface q_l shown in Figure 9. As discussed previously,[48] this observation suggests that long wavelength fluctuations at the surface and interface are conformal, in contrast to the short wavelength behavior discussed below.

The three-stage evolution of the long wavelength fluctuations approximately coincides with the temporal evolution of morphology. Recall that the long wavelength fluctuations are attributed to capillary fluctuations in the trilayer structure, dPMMA-rich/SAN-rich/dPMMA-rich. These fluctuations are due to the attractive interaction between the two interfaces separating the SAN-rich middle layer. The development of the capillary fluctuations between two homogeneous polymer films has been measured previously.[52] In this study, as capillary fluctuations begin to develop, the structure, thickness, composition, and homogeneity of the middle layer are changing. In particular, the middle layer transforms from a bicontinuous structure to one with dPMMA-rich columns spanning the wetting layers, decreases and then increases its thickness, increases and then decreases the average SAN composition, and finally increases its heterogeneity. New models reflecting this complex film structure are needed to understand the relationship between long wavelength fluctuations and morphology.

During the intermediate stage, q_l reaches a constant value, suggesting that lateral fluctuations can be pinned. Capillary wave theory for thin films predicts that the wavenumber is independent of time and scales as h_0^{-2}, whereas the amplitude increases with time.[44−46] Figure 9 shows that the plateau wavenumbers, $q_{l,p}$, are 1.8, 0.8, and 0.35 μm^{-1}, for T1, T2, and T5, respectively. On a log−log scale, the inset of Figure 9 shows that $q_{l,p}$ scales as l_0^{-1}. Though this scaling appears similar to the results in ref 23, their proposed mechanism clearly does not apply to our case. Namely, they assume that the lateral length scale of roughening is a direct consequence of phase coarsening (i.e., the evolution of one length scale); however, we demonstrate here and previously[25,48] that roughening occurs by two distinct mechanisms: short wavelength fluctuations associated with phase separation and long ones due to capillary fluctuation. We note that the A/B/A structure in the primitive capillary fluctuation model is much simpler than our experimental system where B contains two phases and a time-dependent thickness. Further theoretical development is necessary.

The late stage reflects macroscopic roughening. Although q_l remains constant during the intermediate stage, the amplitude of the pinned capillary fluctuation increases and eventually ruptures the film. The rupture time, t_r, is determined at the crossover between the plateau and late stage power law behavior as shown in Figure 9. The values for t_r are given in Table 1. During this stage, q_l describes the coarsening of the middle layer as it evolves from a lacy, interconnected 2D network (e.g., Figure 4f) to isolated droplets (e.g., Figure 4h). In a relevant study, Sung et al. reported a $t^{-0.44}$ power law for 2D phase separation in thin films.[5] For films from 100 to 500 nm, we observe that the dominant q scales as $t^{-1/3}$ for relatively thick films. However, for thin films on the order of the chain size, q follows a $t^{-0.25}$ power law.[38]

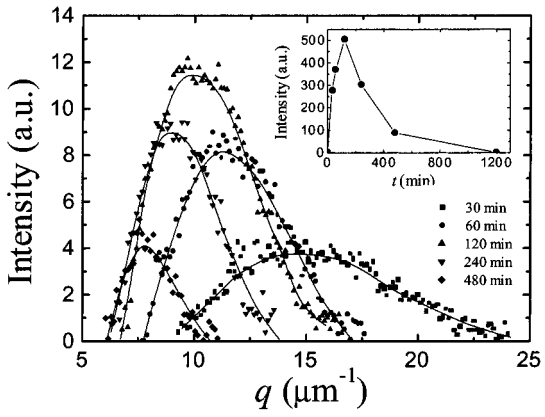

Figure 10. Intensity of q_h for T2 after 30 (squares), 60 (circles), 120 (up-triangles), 240 (down-triangles), and 480 min (diamonds). The background is subtracted as shown in Figure 8. The solid curves are the best fits to the data. Note that the uncertainty of the peak position is larger than the adjacent intervals which is defined by the size of the image or the cutoff effect. The inset shows the integrated intensity of the q_h peaks.

3.3. High Wavenumber Fluctuations, q_h. At the free surface, the short wavelength features appear as small hills as shown in Figures 2a and 4c, whereas at the interface, this structure appears as the small depressions shown in Figures 2b and 4d. By analyzing the intensity and peak position of the FFT, surface hills are shown to evolve by a unique pattern. Figure 10 shows the intensity of the short wavelength peaks at the surface of T2 after 30, 60, 120, 240, and 480 min. The solid lines are the best fits to the data. Each spectrum shows a maximum intensity at $q_{h,s}$, the characteristic wavenumber of the surface features. Initially, the peak intensity increases with time, reaches a maximum at 120 min, and then decreases. Note that $q_{h,s}$ shifts continuously toward lower q, consistent with coarsening of the lateral features. The inset shows the peak integrated intensity as a function of time. Similar to peak height, the intensity increases rapidly, reaches a maximum value at 120 min, and then decays.

The $q_{h,s}$ peak reflects the dynamics of the surface hill during the early and intermediate stages of morphology evolution. At early times, because of hydrodynamic flow of the wetting component toward the surface, surface hills are created as a consequence of balancing the capillary pressure at the surface.[24] The periodicity of the hills reflects the internal structure and the degree of the hydrodynamic wetting process. Thus, $q_{h,s}$ corresponding to the peak intensity reflects a well-ordered arrangement of hills and coincides with the onset of the first roughness plateau. Upon further annealing, the internal pressure responsible for hydrodynamic-flow driven wetting vanishes, and the net capillary pressure reverses its direction toward the middle of the film, causing the hills to collapse. High-resolution images of collapsed hills have been published.[25]

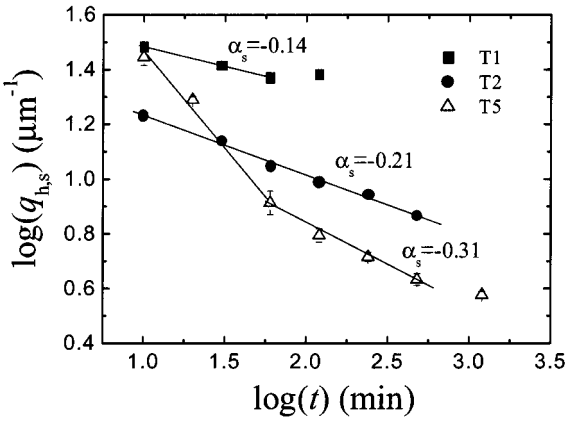

Figure 11. High-q peak at the surface, denoted as $q_{h,s}$, is plotted as a function of time on a log−log plot for T1 (solid squares), T2 (solid circles), and T5 (open triangles). For all samples, power law behavior was observed. T5 shows a crossover from a fast to slow behavior. Note that some error bars for the filled symbols are smaller than the symbol size itself.

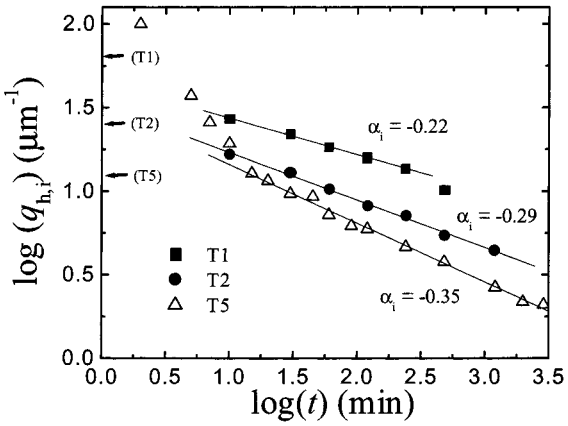

Figure 12. High-q peak at the interface, denoted as $q_{h,i}$, is plotted as a function of time on a log−log plot for T1 (solid squares), T2 (solid circles), and T5 (open triangles). The arrows indicate values of $\log(q_t) = \log(2\pi/l_0)$ which are 1.8, 1.4, and 1.1, respectively. For all samples, power law behavior was observed. T5 shows a crossover from fast to slow behavior.

Figure 11 shows the evolution of $q_{h,s}$ for T1, T2, and T5. The solid lines are linear fits, suggesting power law behavior, $q_h \sim t^{\alpha}$. For T5, the short wavelength features display a crossover from fast to slow growth. This crossover coincides with a transition from 3D to 2D behavior, which occurs when feature size approaches the film thickness.[25] Both T1 and T2 display single power law behavior. As discussed below, the fast growth regime observed for T5 may have occurred too quickly for these thin samples. For comparison, the wavenumbers corresponding to the initial film thickness, $q_t = 2\pi/l_0$, of T1, T2, and T5 are 58, 28, and 13 μm^{-1}, respectively, or a $\log(q_t)$ of 1.8, 1.4, and 1.1. As shown in Figure 11, the values of $\log(q_{h,s})$ are less than 1.8 and 1.4 for T1 and T2, respectively, suggesting that experiments would need to be performed at much earlier times to capture the crossover. Note that 1.1 lies in the middle of the $\log(q_{h,s})$ range for T5. Because of the small length scale and fast kinetics, measurements of $q_{h,s}$ at shorter times were not possible for T1 and T2. In the 2D regime, the power law exponent at the surface, α_s, increases from −0.14 to −0.31 as l_0 increases from 108 to 495 nm.

The characteristic wavenumber for interfacial fluctuations $q_{h,i}$ is shown in Figure 12 for T1, T2, and T5. As a reference, the arrows denote q_t. Similar to the surface characteristics, the interfacial wavenumber undergoes a crossover from fast to slow power law behavior for T5, whereas a single power law is observed for T1 and T2. As before, the crossover can be attributed to the 3D to 2D transition due to film confinement. For each sample, a comparison of Figures 11 and 12 shows that the values of $q_{h,i}(t)$ are less than $q_{h,s}(t)$, indicating that interfacial fluctuations develop faster than surface fluctuations. For T1 and T2, the magnitudes of $q_{h,s}$ and $q_{h,i}$ are similar at early times but diverge at late times according to different power laws. In the 2D regime, the power law exponent of the interface, α_i, increases from −0.21 to −0.35 as l_0 increases from 108 to 495 nm.

These studies show that thin film confinement affects both the magnitude and growth rate of surface and interface compositional fluctuations parallel to the surface. For dPMMA:SAN at 185 °C, the bulk correlation length is much less than the thinnest film (∼100 nm), so, initially, coexisting phases grow in 3D. As the phase domains continue to grow, their size normal to the film, R_n, approaches the middle layer thickness h and becomes confined; however, the lateral size of the domain, R_h, can continue to grow in 2D. The transition from 3D to 2D growth is manifested as a change in kinetics.[25] Before the transition, R_h and R_n are similar in magnitude while $R_h > R_n$.[32−37] Because it is difficult to quantify R_n, the crossover criterion $R_n \sim h$ is approximated by $R_h \sim l_0$. This relationship provides a convenient measure of the crossover point. Figure 12 shows that for T5 the crossover occurs after 15 min at $\log(q_{h,i}) = 1.1$, which is very close to $\log(q_t)$ (cf. arrows). The crossover times for T1 and T2 can be estimated by extrapolation and found to be 0.3 and 2 min, respectively. These times provide a prediction for the 3D to 2D transition in those films. The dynamics of surface features differ from those at the interface. Note that the crossover time for T5 occurs much later at the surface (∼60 min) than the interface (∼15 min) and at a larger characteristic length (∼0.8 μm). These differences are further discussed below.

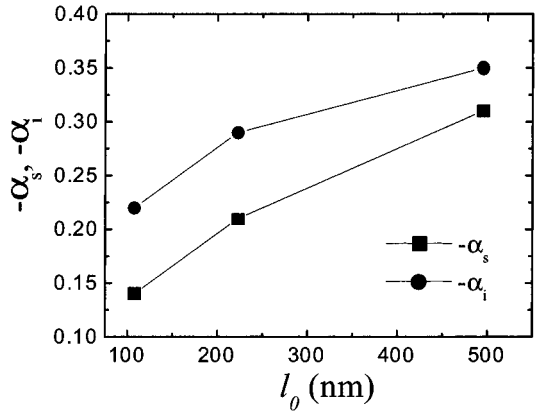

Figure 13. Magnitude of the power exponents of q_h at both the surface ($-\alpha_s$) and interface ($-\alpha_f$) as a function of film thickness. Both exponents approach an asymptotic value of $^1/_3$ as thickness increases.

Figures 11 and 12 demonstrate that q_h follows the power law behavior $q_h \sim t^{\alpha}$ during 2D coarsening, with a power exponent, α, depending on both film thickness and depth. Figure 13 shows that the magnitude of the surface and interface exponents, $-\alpha_s$ and $-\alpha_i$, increases

with film thickness. Although data are limited, both exponents increase and approach an asymptotic value of about $^1/_3$ as l_0 increases. This observation is different from a previous simulation which predicts that film thickness has little effect on lateral growth kinetics.[32] This discrepancy is presumably due to different phase coarsening mechanisms: a diffusive motion in the simulation and hydrodynamics in the current study. Moreover, $-\alpha_i$ is systematically larger than $-\alpha_s$, indicating that internal dynamics is more rapid than that at the surface. This result provides the first experimental evidence for depth dependence of phase separation kinetics predicted by numerical simulations.[36] While numerical methods allow for the determination of the lateral correlations at any depth from the surface, our experiments conveniently provide measurements at both the surface and the interface between the wetting and nonwetting layer. The surface correlation is not accessible by simulations which typically assume rigid walls at both surfaces, rather than a surface that can deform. However, correlations at the interface correspond to the morphology at the first zero in a depth profile of the order parameter and therefore may be directly compared with simulations.

Prior experimental studies have also investigated the kinetics of phase separating polymer blends in a confined geometry. Selected comparisons between these experiments and the present one are described. Pan and Composto[2] reported phase separation in thin films of polystyrene (PS) and poly(vinyl methyl ether) confined between two glass slides. Although phase growth is inhibited by confinement, strong wetting and the hard wall boundaries prevent film roughening. Bruder et al.[13,14] reported phase separation in PS/poly(styrene-*co*-bromostyrene) (PBr_xS) blends. The growth of the relevant lateral dimension corresponds to the intermediate stage of their study, when the wetting component flows from the surface into growing domains.[14] Films remained smooth, and therefore no late stage evolution was reported. Both the lateral domain dimension and wetting layer thickness followed $t^{1/3}$ kinetics. Although their growth exponent is similar to ours, a direct comparison is problematic because we report the correlation between domains (cf. Figure 8) rather than domain size. Sung et al.[5] reported lateral growth that follows a $t^{0.44}$ power law. However, their regime of study corresponds to late stage growth. Tanaka and co-workers[3,4] have investigated phase separation under 1D and 2D confinement. Similar to our observations during the early and intermediate stages of morphology evolution, they observe hydrodynamic flow driven wetting followed by back-flow from the wetting layer. By measuring the depth profiles, surface-directed, spinodal decomposition in semiinfinite films[8,9] and finite films displaying confinement-induced interference have been investigated.[10,12] These measurements underlie the behavior of the current study during the early and intermediate regimes of morphology evolution.[25] Wiltzius and Cumming revealed a fast surface-directed mode ($q \sim t^{-\alpha}$, where $1.0 < \alpha < 1.5$),[49] which was eventually attributed to 2D coarsening of the wetting phase against the confining wall.[50,51] Geoghegan et al. observed a transition of the wetting layer growth from $t^{1/3}$ to logarithmic to $t^{1/2}$ as a function of decreasing quench depth.[22] For the $t^{1/3}$ regime, surface roughness was attributed to droplets of the wetting phase at the surface.

In addition to experiments, numerical simulations provide some guidelines for understanding the early and intermediate stages.[32−37] For polymer blends near a weak attractive wall and diffusion-limited growth, phases are predicted to grow as $t^{1/3}$ both parallel and perpendicular to the wall.[32,35−37] Furthermore, surface retardation can produce an anisotropic phase morphology as well as depth-dependent growth behavior.[32,36] Presently, the discrepancy between the experimental fast wetting kinetics[3,24] and simulations (strong wetting conditions) is expected because the latter do not capture the late stage morphology nor include hydrodynamic flow and a deformable free surface. Simulations that allow for surface deformation[53] and hydrodynamic flow[54] have been introduced and may be extended to this study.

As mentioned in the Introduction and discussed above, simulations and experimental studies are difficult to compare because they usually cover different time regimes. Whereas the former apply to the early time regime, experimental studies mainly focus on the intermediate and late regimes. Within the framework of class A type evolution, we emphasize that the current experiments cover all time regimes, and 3 decades of time, allowing for a direct comparison between measurement and simulation. This article provides a comprehensive study of the identification and quantification of the length scales at the polymer surface as well as the interface between the wetting and nonwetting phase. We observe a lateral phase growth rate that approaches $t^{1/3}$ as confinement relaxes and depends on depth, consistent with the numerical simulations.[32−37] Direct comparison between experiments and simulations is not yet available for the long wavelength fluctuations and late stage coarsening. However, recent Lattice−Boltzmann (LB) simulations of phase separation in the presence of surface enriching boundaries was able to capture layer formation at early times and a subsequent capillary instability,[55] suggesting that LB simulations are a promising approach to understand the complex behavior of phase separating polymer blend films.

Conclusion

Phase separating dPMMA/SAN thin films ranging from 10 to 150 R_g display three distinct stages of evolution as described previously. In this article, we investigate the effect of confinement on the dynamics of roughness and the lateral length scales induced by capillary fluctuations and spinodal decomposition. During the early and intermediate stages, surface roughness can be attributed to phase separation and capillary fluctuations. However, roughness increases much faster than predictions based on simple capillary fluctuation theory. The late stage of roughening is complicated by many factors, including phase coarsening, capillary fluctuations, wetting, and hydrodynamic interactions and is not described by simple scaling rules. The surface and interface fluctuations are followed using AFM. The lateral length scales of these fluctuations generally follow power law dynamics but also depend on confinement and depth. For both the surface and interfacial lateral features, the growth rates increase, and the power law exponents approach $^1/_3$ as film thickness increases. Furthermore, the surface kinetics is consistently slower than the interface, suggesting a surface retarding effect and decoupling between the surface and

internal features. These results point to the important roles played by surface roughening and hydrodynamics during spinodal decomposition in polymer thin films and, hopefully, pose a challenge for future experiments, simulations, and theories.[23,56,57]

Acknowledgment. We acknowledge primary financial support from NSF DMR program, Grant DMR-9974366. Partial support and shared experimental facilities support were provided by the NSF MRSEC program, Grant NSF DMR00-79909. We acknowledge stimulating discussions with Dr. Charles C. Han and Prof. Tom C. Lubensky.

References and Notes

(1) Binder, K. *J. Non-Equilib. Thermodyn*. **1998**, *23*, 1 and references therein.
(2) Pan, Q.; Composto, R. J. *Mater. Res. Soc. Symp. Proc.* **1995**, *366*, 27.
(3) Tanaka, H. *Phys. Rev. Lett.* **1993**, *70*, 53. (b) Tanaka, H. *Phys. Rev. Lett.* **1993**, *70*, 2770. Tanaka, H.; Lovinger, A. J.; Davis, D. D. *Phys. Rev. Lett.* **1994**, *72*, 2581.
(4) Tanaka, H. *Phys. Rev. E* **1995**, *51*, 1313. Tanaka, H.; Sigehuzi, T. *Phys. Rev. E* **1995**, *52*, 829.
(5) Sung, L.; Karim, A.; Douglas, J. F.; Han, C. C. *Phys. Rev. Lett.* **1996**, *76*, 4368.
(6) Ribbe, A. E.; Hayashi, M.; Weber, M.; Hashimoto, T. *Polymer* **1998**, *39*, 7149.
(7) Haas, C. K.; Torkelson, J. M. *Phys. Rev. E* **1997**, *55*, 3191.
(8) Jones, R. A. L.; Norton, L. J.; Kramer, E. J.; Bates, F. S.; Wiltzius, P. *Phys. Rev. Lett.* **1991**, *66*, 1326.
(9) Krausch, G.; Dai, C.; Kramer, E. J.; Bates, F. K. *Phys. Rev. Lett.* **1993**, *71*, 3669.
(10) Krausch, G.; Kramer, E. J.; Bates, F. K.; Marko, J. F.; Brown, G.; Chakrabarti, A. *Macromolecules* **1994**, *27*, 6768.
(11) Krausch, G.; Dai, C.; Kramer, E. J.; Marko, J. F.; Bates, F. K. *Macromolecules* **1993**, *26*, 5566.
(12) Genzer, J.; Kramer, E. J. *Phys. Rev. Lett.* **1997**, *78*, 4946; *Europhys. Lett.* **1998**, *44*, 180.
(13) Bruder, F.; Brenn, R. *Phys. Rev. Lett.* **1992**, *69*, 624.
(14) Straub, W.; Bruder, F.; Brenn, R.; Krausch, G.; Bielefeldt, H.; Kirsch, A.; Marti, O.; Mlynek, J.; Marko, F. *Europhys. Lett.* **1995**, *29*, 353.
(15) Karim, A.; Slawecki, T. M.; Kumar, S. K.; Douglas, J. F.; Satija, S. K.; Han, C. C.; Russell, T. P.; Liu, Y.; Overney, R.; Sokolov, J.; Rafailovich, M. H. *Macromolecules* **1998**, *31*, 857.
(16) Kajiyama, T.; Tanaka, K.; Ohki, I.; Ge, S.; Yoon, J.; Takahara, A. *Macromolecules* **1994**, *27*, 7923.
(17) Muller-Buschbaum, P.; Vanhoorne, P.; Scheumann, V.; Stamm, M. *Europhys. Lett.* **1997**, *40*, 655.
(18) Ermi, B. D.; Karim, A.; Douglas, J. F. *J. Polym. Sci., Part B: Polym. Phys.* **1998**, *36*, 191.
(19) Jandt, K. D.; Heier, J.; Bates, F. S.; Kramer, E. J. *Langmuir* **1996**, *12*, 3716.
(20) Heier, J.; Kramer, E. J.; Revesz, P.; Battistig, G.; Bates, F. S. *Macromolecules* **1999**, *32*, 3758.
(21) Tanaka, K.; Yoon, J.; Takahara, A.; Kajiyama, T. *Macromolecules* **1995**, *28*, 934.
(22) Geoghegan, M.; Ermer, H.; Jungst, G.; Krausch, G.; Brenn, R. *Phys. Rev. E* **2000**, *62*, 940.
(23) Hoppe, H.; Heuberger, M.; Klein, J. *Phys. Rev. Lett.* **2001**, *86*, 4863.
(24) Wang, H.; Composto, R. J. *Phys. Rev. E* **2000**, *61*, 1659.
(25) Wang, H.; Composto, R. J. *Europhys. Lett.* **2000**, *50*, 622; *J. Chem. Phys.* **2000**, *113*, 10386.
(26) Flebbe, T.; Dunweg, B.; Binder, K. *J. Phys. II* **1996**, *6*, 667.
(27) Binder, K.; Nielaba, P.; Pereyra, V. Z. *Phys. B* **1997**, *104*, 81.
(28) Binder, K. *Acta Polym.* **1995**, *46*, 204.
(29) Reich, S.; Cohen, Y. *J. Polym. Sci., Phys.* **1981**, *19*, 1255. Jones, R.; Kumar, S. K.; Ho, D.; Briber, R.; Russell, T. P. *APS Bull.* **2000**, *45*, 375.
(30) Zhu, S.; Liu, Y.; Rafailovich, M. H.; Sokolov, J.; Gersappe, D.; Winesett, D. A.; Ade, H. *Nature (London)* **1999**, *400*, 49.
(31) Keblinski, P.; Kumar, S. K.; Maritan, A.; Koplik, J.; Banavar, J. R. *Phys. Rev. Lett.* **1996**, *76*, 1106.
(32) Puri, S.; Binder, K. *J. Stat. Phys.* **1994**, *77*, 145.
(33) Frisch, H. L.; Nielaba, P.; Binder, K. *Phys. Rev. E* **1995**, *52*, 2848.
(34) Binder, K.; Muller, M. *Macromol. Symp.* **2000**, *149*, 1.
(35) Marko, J. F. *Phys. Rev. E* **1993**, *48*, 2861.
(36) Puri, S.; Binder, K. *Z. Phys. B: Condens. Mater.* **1992**, *86*, 263. Puri, S.; Binder, K. *Phys. Rev. A* **1992**, *46*, R4487. Puri, S.; Binder, K. *Phys. Rev. E* **1994**, *49*, 5359.
(37) Brown, G.; Chakrabarti, A. *Phys. Rev. A* **1992**, *46*, 4829. Chen, H.; Chakrabarti, A. *Phys. Rev. E* **1997**, *55*, 5680.
(38) Wang, H.; Composto, R. J., to be published.
(39) Ermi, B. D.; Nisato, G.; Douglas, J. F.; Rogers, J. A.; Karim, A. *Phys. Rev. Lett.* **1998**, *81*, 3900. Nisato, G.; Ermi, B. D.; Douglas, J. F.; Karim, A. *Macromolecules* **1999**, *32*, 2356.
(40) Newby, B. M. Z.; Composto, R. J. *Macromolecules* **2001**, *33*, 3274.
(41) Böltau, M.; Walheim, S.; Mlynek, J.; Krausch, G.; Steiner, U. *Science* **1998**, *391*, 877.
(42) Fukunaga, K.; Elbs, H.; Krausch, G. *Langmuir* **2000**, *16*, 3474.
(43) Affrossman, S.; Stamm, M. *Colloid Polym. Sci.* **2000**, *278*, 888. Muller-Buschbaum, P.; Gutmann, J. S.; Stamm, M. *Macromolecues* **2000**, *33*, 4886; *Colloid Polym. Sci.* **1999**, *277*, 193.
(44) Vrij, A. *Discuss. Faraday Soc.* **1966**, *42*, 23.
(45) Vrij, A.; Overbeek, J. Th. G. *J. Am. Chem. Soc.* **1968**, *90*, 3074.
(46) Brochard, F.; Daillant, J. *Can. J. Phys.* **1990**, *68*, 1084.
(47) Xie, R.; Karim, A.; Douglas, J. F.; Han, C. C.; Weiss, R. *Phys. Rev. Lett.* **1998**, *81*, 1251.
(48) Wang, H.; Composto, R. J.; Hobbie, E. K.; Han, C. C. *Langmuir* **2001**, *17*, 2857.
(49) Wiltzius, P.; Cumming, A. *Phys. Rev. Lett.* **1991**, *66*, 3000. Cumming, A.; Wiltzius, P.; Bates, F. S.; Rosedale, J. H. *Phys. Rev. A* **1992**, *45*, 885.
(50) Troian, S. M. *Phys. Rev. Lett.* **1993**, *71*, 1399.
(51) Tanaka, H. *Phys. Rev. E* **1996**, *54*, 1709.
(52) Sferrazza, M.; Xiao, C.; Jones, R. A. L.; Bucknall, D. G.; Webster, J.; Penfold, J. *Phys. Rev. Lett.* **1997**, *78*, 3693. Sferrazza, M.; Xiao, C.; Jones, R. A. L.; Penfold, J. *Philos. Magn. Lett.* **2000**, *80*, 561.
(53) Kotelyanskii, M.; Kumar, S. K. *Phys. Rev. Lett.* **1998**, *80*, 1252.
(54) Tanaka, H.; Araki, T. *Phys. Rev. Lett.* **1998**, *81*, 389.
(55) Martys, N.; Douglas, J. F. *Phys. Rev. E*, in press.
(56) Rysz, J.; Ermer, H.; Budkowski, A.; Bernasik, A.; Lekki, J.; Juengst, G.; Brenn, R.; Kowalski, K.; Camra, J.; Lekka, M.; Jedlinski, J. *Eur. Phys. J. E* **2001**, *5*, 207.
(57) Tanaka, H. *J. Phys.: Condens. Matter* **2001**, *13*, 4637.

MA0116699